

High-order solar migrating tides quench at SSW onsets

Maosheng He¹, Jeffrey M. Forbes², Jorge L.Chau¹, Guozhu Li³, Weixing
Wan³, Dmitry V. Korotyshkin⁴

¹Leibniz-Institute of Atmospheric Physics at the Rostock University, Kühlungsborn, Germany

²Ann & H.J. Smead Department of Aerospace Engineering Sciences, University of Colorado, Boulder,
USA

³Key Laboratory of Earth and Planetary Physics, Institute of Geology and Geophysics, Chinese Academy
of Sciences, Beijing, China

⁴Kazan Federal University, Kazan, Russia

Key Points:

- First six solar tidal harmonics occur in the mesospheric wind during SSW 2018 among which the 4th, 5th, and 6th harmonics quench at the SSW onset.
- Wavenumber diagnosis using multi-station techniques suggests all six harmonics are dominated by migrating tides.
- In a near-12-year statistics, the six harmonics and quenching also occur.

Corresponding author: M. He, he@iap-kborn.de

Abstract

Sudden stratospheric warming events (SSWs) are the most spectacular atmospheric vertical coupling processes, well-known for being associated with diverse wave activities in the upper atmosphere and ionosphere. The first four solar tidal harmonics have been reported as being engaged. Here, combining mesospheric winds detected by three mid-latitude radars, we demonstrate at least the first six harmonics occur during SSW 2018. Wavenumber diagnosis demonstrates that all six harmonics are dominated by migrating components. Wavelet analyses reveal that the 4th, 5th, and 6th harmonics quench after the SSW onset. The six harmonics and the quenching appear also in a statistical analysis based on near-12-year observations from one of the radars. We attribute the quenching to reversal of the background eastward wind.

Plain Language Summary

Solar tides are the most predictably-occurring waves in the upper atmosphere. Although the dynamical theory can be dated back to Laplace in the 16th century, upper atmospheric tides were rarely studied observationally until satellites and ground-based radars became common. To date, observational studies have mainly dealt with low-order solar-day harmonics. Here, we combine mesospheric wind observations from three longitudinal sectors to investigate high-order harmonics. Results illustrate that the first six harmonics appear in early 2018, all of which are dominated by sum-synchronous components. Among these harmonics, the 4th, 5th, and 6th quench at the sudden stratospheric warming onset, which we attribute to variations in the background zonal wind.

1 Introduction

Solar tides are excited by heating due to the diurnal cycle of solar radiation absorption by various chemical species throughout the atmosphere, as well as the release of latent heat associated with convection in the troposphere. There is also substantial evidence that solar tides can also be produced by nonlinear interactions between various tidal components, and between tides and stationary planetary waves. Readers are referred to Truskowski et al. (2014) for a review of how various observed migrating (sun-synchronous) and non-migrating tides are thought to be excited. The diurnal cycle of heating generates a series of solar harmonics (designated in this paper as S1, S2, ..., S7

47 corresponding to periods of 24hr, 12hr, ..., 24/7hr). Harmonics at least up to S7 were
48 observed in the low atmospheric meteorological observations (e.g., Hedlin et al., 2018),
49 most of which exist also in the upper atmosphere as illustrated in the power spectral den-
50 sity of multi-year observations of mid-latitude mesospheric wind, in Figure S1 in the sup-
51 porting information. Based on numerous modeling efforts and data analyses since the
52 early work of Lindzen and Hong (1974), it is now known that at least for S1 to S4 the
53 atmosphere responds in a quasi-linear fashion to each of these harmonics separately.

54 Most of the tidal literature is devoted to data analyses, modeling, and interpreta-
55 tion of S1, S2, and S3. Recently, S4 has received some attention in terms of ground-based
56 observations (e.g., Guharay et al., 2018; Jacobi et al., 2017; Smith et al., 2004), space-
57 based observations (e.g., Azeem et al., 2016; Xu et al., 2012; M. H. Liu et al., 2015) and
58 modeling (e.g., Geissler et al., 2019; Smith et al., 2004). The ground-based observations
59 have the advantage of high temporal resolution, but cannot distinguish between migrat-
60 ing and non-migrating tidal components from single-station measurements. On the other
61 hand, tidal determinations from single-spacecraft observations provide a global view but
62 one that is typically an average over periods of order 30-60 days, and thus subject to un-
63 derestimation due to phase cancellation effects. With respect to harmonics at higher or-
64 ders, to our knowledge, the only modeling and observational investigation pertaining to
65 S5 and S6 was performed by Miyoshi et al. (2009) in the context of solar terminator waves.

66 In the present paper we employ a special technique to identify migrating tides S2-
67 S6 from three radars separated in longitude at a near-constant latitude of $\sim 55^\circ\text{N}$, and
68 thus eliminate some of the shortcomings noted above. We furthermore pursue this in the
69 context of the behaviors of S2-S6 during the stratosphere sudden warming (SSW) of 2018.
70 SSWs are the most spectacular meteorological processes of the atmospheric vertical cou-
71 pling, in which the polar vortex is destroyed in a couple of days (e.g., Scherhag, 1952;
72 Reed, 1963). SSWs are associated with diverse wave activities in the upper atmosphere
73 and ionosphere, including planetary waves, gravity waves, and lunar and solar tides (e.g.,
74 Chau et al., 2012; Pedatella & Forbes, 2010). Among the solar tides, variations of the
75 first four harmonics were reported, among which S2 has attracted most intensive atten-
76 tion. Early results on S2 exhibited a contradiction. Some reported an increase during
77 SSWs (e.g., according to TIMEGCM model H. L. Liu et al., 2010) while others shown
78 a decrease (e.g., according to WAM model in Fuller-Rowell et al., 2011). Later studies
79 with zonal wavenumber constraint suggested that the migrating component decreases

(at least after the SSW onset and at mid- and high- latitude, e.g., He & Chau, 2019; Hibbins et al., 2019) whereas two non-migrating components enhance (e.g., Smith, 2012; Xiong et al., 2013). Recently, high-frequency-resolved spectral analyses with zonal wavenumber constraint suggested that the enhancements of the non-migrating components are just aliasing of secondary waves of nonlinear interactions between the migrating tides and traveling planetary waves (He, Chau, Stober, et al., 2018; He & Chau, 2019).

In addition to the responses of S2, enhancements of S3 and S4 were also reported during SSWs (e.g., Gong & Zhou, 2011; Gong et al., 2018). The S3 and S4 enhancements were detected using single-station approaches and therefore it is still not clear that are they associated with migrating or non-migrating components. The first purpose of the current work is to implement the multi-station approach to diagnose the zonal wavenumbers of S3 and S4 signatures during SSWs. We are also aim to explore the behaviors of higher order solar tidal harmonics during SSWs.

For the above purposes, we investigate the mesospheric wind observations collected by three meteor radars in three longitudinal sectors during SSW 2018. Figure S2 in the supporting information displays the distribution of the radars, at Juliusruh (53.5°N,122.3°E), Mohe (53.5°N,122.3°E), and Kazan (55.7°N,49°E) (readers are referred to Singer et al., 2013; Yu et al., 2013; Korotyshkin et al., 2019, for the radar frequencies, antenna configurations, and other setups). Combining three radars allows us to diagnose the horizontal scale of the tides. Among the radars, the one at Juliusruh collected continuous observations for more than 12 years, which will be used for a multi-year statistic study.

2 Results

In Section 2.1, we diagnose the dominant zonal wavenumber of tidal harmonics in SSW 2018 through a phase differencing approach (developed in He, Chau, Stober, et al., 2018), and explore the temporal evolution of the harmonics during SSWs through wavelet analysis in Section 2.2.

2.1 Zonal wavenumber diagnosis

Figure 1a displays the Lomb-Scargle spectra of the zonal wind at 90 km altitude during SSW 2018, between 01 January and 31 March 2018. The three colors represent the three radars. At the first six harmonics, $f=1,2,\dots,6$ cpd, peaks occur above the sig-

110 nificant level $\alpha = 0.01$. At each individual harmonic the three complex amplitudes are
 111 combined to diagnose the zonal wavenumber m of the underlying wave through two ap-
 112 proaches, the dual- and triple-station approaches detailed in Appendices A1 and A2, re-
 113 spectively. The corresponding dual- and triple-station results are denoted as \hat{m}_k^D ($k=1,2,3$
 114 denotes three combinations of radar pairs) and \hat{m}^T , illustrated in Figure 1b as the col-
 115 ored and white symbols, respectively. The shape of the colored symbols represents dif-
 116 ferent whole cycles in-between each radar pair. For example, the longitudinal separation
 117 between Kazan and Juliusruh is shorter than wavelengths at all harmonics, whereas that
 118 between Mohe and Juliusruh is shorter than the wavelengths only at the first two har-
 119 monics. In Figure 1b, the black dashed line denotes the isoline of sun-synchronous phase
 120 velocity $v_p \equiv f/m = \Omega := 1\text{cpd}$. The estimated wavenumber $\hat{m}_k^D(f)$ and $\hat{m}^T(f)$ con-
 121 sistently distribute along the dashed line, suggesting that the underlying waves at all har-
 122 monics are dominantly sun-synchronous, namely, migrating components associated with
 123 zonal wavenumber $m_s(f) = f/\Omega$.

124 2.2 Quenching of high-order tidal harmonics during SSW

125 The current Section investigates the temporal evolution of the harmonics in the win-
 126 dow in which data are used in Figure 1. We carry out Morlet wavelet at each altitude
 127 and station, and average the resultant spectra in the altitude range $80 < h < 100$ km.
 128 The average spectra for the three radars are displayed in Figures 2a-c, respectively. The
 129 spectra share the following characters. S2 is almost always the most dominant harmonic,
 130 whereas S3, S4, S5 and S6 also occur unstably with short time variabilities. The vari-
 131 abilities are potentially due to interactions with planetary waves (e.g., Pancheva et al.,
 132 2002; He et al., 2017), gravity waves (e.g., Miyahara & Forbes, 1991) or other tidal com-
 133 ponents (e.g., Lilienthal & Jacobi, 2019). The high order harmonics, e.g., S4, S5, and
 134 S6, occur stronger or more often before the SSW onset (displayed as the magenta line,
 135 referring to the central day of polar vortex weakening, PVW, cf., Zhang & Forbes, 2014)
 136 than after the onset. For comparison, the three spectra are averaged in two time win-
 137 dows displayed by the blue and red horizontal bars before and after the onset in Figures 2a-
 138 c. The average, displayed in Figure 2e, exhibits the most significant difference at S4, S5,
 139 and S6 which are suppressed or quenched after the onset. S6 quenches by about 2/3 ac-
 140 cording to the ratio shown in Figure 2f.

141 For a statistical perspective, the same wavelet analysis is implemented on the near-
142 12-year data used in Figure S1, generating an altitude-averaged spectrum similar to Fig-
143 ure 2c but for the period between January 01, 2007 and March 03, 2019. The spectral
144 intensity is averaged with respect to all SSW onsets (referring to PVWs). Such an av-
145 erage is called composite analysis (CA) or superposed epoch analysis. The CA result is
146 displayed in Figure 3a, and its altitude structure, averaged within the time window in-
147 dicated by the blue horizontal bar in Figure 3a, is displayed in Figure 3b. Similar to Fig-
148 ures 2a-c, in Figures 3a and 3b the first six harmonics occur, all of which increase with
149 altitude exponentially. Among the harmonics, S4, S5 and S6 quench or weaken around
150 the onset. In addition to the quenched harmonics, S2 exhibits, in both Figure Figures
151 2e and 3c, a weakening after the onset, which is out of our focus hereafter given that the
152 S2 weakening has been reported and discussed individually (Hibbins et al., 2019; He &
153 Chau, 2019).

154 **3 Discussions**

155 In this paper we report the quenching of high-order migrating tides in connection
156 with SSW onset. The existence of migrating tides under undisturbed winter conditions
157 at middle to high latitudes is not surprising. Linear tidal modeling of S2 taking into ac-
158 count forcing by ozone heating alone (Hagan et al., 1999) shows that the tidal amplitudes
159 in zonal wind are significantly enhanced between 75-100 km at the poleward of 30° lat-
160 itude in the winter hemisphere (January and July for the northern and southern hemi-
161 spheres, respectively) compared to the summer hemisphere where the maximum heat-
162 ing occurs. This is due in part to the Doppler-shifting of westward-propagating waves
163 to higher frequencies as they preferentially propagate through prevailing eastward winds
164 with reduced susceptibility to dissipation, and with the Doppler-shifting effect increas-
165 ing with zonal wavenumber. Winter maxima are in fact revealed for S2, S4, S5 and S6
166 in Figure 4, which displays the similar plot as 3a, but averaged with respect to calen-
167 dar date. The existence of significant amplitudes for S2 and S3 during non-winter months
168 in Figure 4 likely reflects the importance of tropospheric sources and tide-tide nonlin-
169 ear interactions, which were not considered by Hagan et al. (1999). In addition, ozone
170 heating also plays a role. As shown by Xu et al. (2012), while maximum forcing of S2
171 and S4 occur in the winter hemisphere, that of S3 occurs in the summer hemisphere.

172 The above simple picture of seasonal variations is significantly disrupted during SSWs.
 173 With respect to tidal quenching at the SSW onset, a potential explanation is the vari-
 174 ation of the background zonal flow which is prevailingly eastward and reverses to west-
 175 ward during SSWs (e.g., McLandress, 2002). In addition, the linearized momentum equa-
 176 tions contain terms dependent on the meridional and vertical gradients of the mean zonal
 177 wind (Hagan et al., 1999), which might be expected to assume significant importance
 178 compared to the above seasonal effects during SSWs. Figure 3d displays low-passed fil-
 179 tered zonal winds at the three radars. At all radars, the wind is eastward before the on-
 180 set but westward after that, and decreases by 40-60m/s, from the maximum immediate
 181 before the onset to the minimum immediately after the onset. The wind reversal might
 182 account for the fact that in Figures 2e and 3c the spectral density, not only at the quenched
 183 tidal frequencies but in the whole range $f > 3\text{cpd}$, is stronger before the onset than af-
 184 ter. This fact suggests that other westward-propagating waves existing before the on-
 185 set, e.g., gravity waves, might also quench after the onset.

186 The reverse of eastward wind was used to explain the S2 weakening after SSW on-
 187 set (Hibbins et al., 2019). Besides its weakening after SSW onset, S2 also exhibits a weak-
 188 ening on a shorter time scale, namely, the S2 minimum at exactly the onset lasting less
 189 than ten days in Figure 3a. This minimum was also reported and attributed to nonlin-
 190 ear interactions with planetary waves (He et al., 2017; He & Chau, 2019). Among all har-
 191 monics above $f \geq 2\text{cpd}$, S3 is an exception which does not respond significantly to
 192 the reversal; the reasons are not obvious. Furthermore, besides the zonal wind, changes
 193 in ozone density (Goncharenko et al., 2012) and accompanying tidal heating might also
 194 alter the magnitudes of migrating tides during SSWs. Evaluation of the roles of ozone
 195 heating and wind variations on the tidal harmonics during SSWs would benefit from global-
 196 scale modeling focused on this topic.

197 4 Summary

198 The current work investigates high order solar tidal harmonics in the mid-latitude
 199 mesospheric wind during SSWs. We present a case study of SSW 2018 using zonal wind
 200 observations from three longitudinal sectors and a statistic study using near-12-year of
 201 observations from a single station. In both studies, occur the first six solar tidal harmon-
 202 ics, among which S4, S5, and S6 signatures enhance before SSW onset and quench at
 203 the onset, potentially due to the enhance and reverse of easterly during SSWs. In the

204 case study and using multi-station approaches, wavenumber diagnosis illustrates that the
 205 dominant components of all harmonics are migrating tides. Our results demonstrate that
 206 the wave activities during SSWs are more diverse than we known.

207 Acknowledgments

208 This work was supported by the Deutsche Forschungsgemeinschaft (DFG, German
 209 Research Foundation) under SPP 1788 (DynamicEarth) projects CH1482/1-2 (DYNAMITE-
 210 2). Jeffrey M. Forbes acknowledges support under NSF Award AGS-1630177 to the Uni-
 211 versity of Colorado. Dmitry V. Korotyshkin acknowledges for the support by RFBR through
 212 grant 18-505-12048. The data from Mohe is provided by BNOSE (Beijing National Ob-
 213 servatory of Space Environment), IGGCAS (Institute of Geology and Geophysics, Chi-
 214 nese Academy of Sciences) through the Data Center for Geophysics, National Earth Sys-
 215 tem Science Data Sharing Infrastructure (<http://wdc.geophys.cn>). Data in this paper
 216 are available at <https://doi.org/10.7910/DVN/KLOGRX>.

217 References

- 218 Azeem, I., Walterscheid, R. L., Crowley, G., Bishop, R. L., & Christensen, A. B.
 219 (2016). Observations of the migrating semidiurnal and quaddiurnal tides from
 220 the RAIDS/NIRS instrument. *J. Geophys. Res. Sp. Phys.*, *121*(5), 4626–
 221 4637. Retrieved from [https://agupubs.onlinelibrary.wiley.com/doi/abs/](https://agupubs.onlinelibrary.wiley.com/doi/abs/10.1002/2015JA022240)
 222 [10.1002/2015JA022240](https://doi.org/10.1002/2015JA022240) doi: 10.1002/2015JA022240
- 223 Chau, J. L., Goncharenko, L. P., Fejer, B. G., & Liu, H.-L. L. (2012). Equato-
 224 rial and low latitude ionospheric effects during sudden stratospheric warming
 225 events : Ionospheric effects during SSW events. *Space Sci. Rev.*, *168*(1-4),
 226 385–417. doi: 10.1007/s11214-011-9797-5
- 227 Clark, R. R., Burrage, M. D., Franke, S. J., Manson, A. H., Meek, C. E., Mitchell,
 228 N. J., & Muller, H. G. (2002). Observations of 7-d planetary waves with
 229 MLT radars and the UARS-HRDI instrument. *J. Atmos. Solar-Terrestrial*
 230 *Phys.*, *64*(8), 1217–1228. Retrieved from [http://www.sciencedirect.com/](http://www.sciencedirect.com/science/article/pii/S1364682602000706)
 231 [science/article/pii/S1364682602000706](http://www.sciencedirect.com/science/article/pii/S1364682602000706) doi: [https://doi.org/10.1016/](https://doi.org/10.1016/S1364-6826(02)00070-6)
 232 [S1364-6826\(02\)00070-6](https://doi.org/10.1016/S1364-6826(02)00070-6)
- 233 Fuller-Rowell, T., Wang, H., Akmaev, R., Wu, F., Fang, T. W., Iredell, M., & Rich-
 234 mond, A. (2011). Forecasting the dynamic and electrodynamic response to the

- 235 January 2009 sudden stratospheric warming. *Geophys. Res. Lett.*, *38*(13). doi:
236 10.1029/2011GL047732
- 237 Geissler, C., Jacobi, C., & Lilienthal, F. (2019). Forcing mechanisms of the quarter-
238 diurnal tide. *Ann. Geophys. Discuss.*, *2019*, 1–24. Retrieved from [https://](https://www.ann-geophys-discuss.net/angeo-2019-145/)
239 www.ann-geophys-discuss.net/angeo-2019-145/ doi: 10.5194/angeo-2019
240 -145
- 241 Goncharenko, L. P., Coster, A. J., Plumb, R. A., & Domeisen, D. I. (2012). The
242 potential role of stratospheric ozone in the stratosphere-ionosphere cou-
243 pling during stratospheric warmings. *Geophys. Res. Lett.*, *39*(8), 1–5. doi:
244 10.1029/2012GL051261
- 245 Gong, Y., Ma, Z., Lv, X., Zhang, S., Zhou, Q., Aponte, N., & Sulzer, M. (2018, dec).
246 A Study on the Quarterdiurnal Tide in the Thermosphere at Arecibo During
247 the February 2016 Sudden Stratospheric Warming Event. *Geophys. Res. Lett.*,
248 *45*(23), 13,142–13,149. Retrieved from [https://onlinelibrary.wiley.com/](https://onlinelibrary.wiley.com/doi/abs/10.1029/2018GL080422)
249 [doi/abs/10.1029/2018GL080422](https://onlinelibrary.wiley.com/doi/abs/10.1029/2018GL080422) doi: 10.1029/2018GL080422
- 250 Gong, Y., & Zhou, Q. (2011). Incoherent scatter radar study of the terdiurnal tide
251 in the E-and F-region heights at Arecibo. *Geophys. Res. Lett.*, *38*(15), 1–5.
252 doi: 10.1029/2011GL048318
- 253 Guharay, A., Batista, P. P., Buriti, R. A., & Schuch, N. J. (2018). On the variability
254 of the quarter-diurnal tide in the MLT over Brazilian low-latitude stations.
255 *Earth, Planets Sp.*, *70*(1), 2337–2344. Retrieved from [https://doi.org/](https://doi.org/10.1016/j.asr.2018.12.037)
256 [10.1016/j.asr.2018.12.037](https://doi.org/10.1016/j.asr.2018.12.037)<https://doi.org/10.1186/s40623-018-0910-9>
257 doi: 10.1186/s40623-018-0910-9
- 258 Hagan, M. E., Burrage, M. D., Forbes, J. M., Hackney, J., Randel, W. J., & Zhang,
259 X. (1999). GSWM-98: Results for migrating solar tides. *J. Geophys. Res. Sp.*
260 *Phys.*, *104*(A4), 6813–6827. doi: 10.1029/1998ja900125
- 261 He, M., & Chau, J. L. (2019). Mesospheric semidiurnal tides and near-12 h waves
262 through jointly analyzing observations of five specular meteor radars from
263 three longitudinal sectors at boreal midlatitudes. *Atmos. Chem. Phys.*, *19*(9),
264 5993–6006. Retrieved from <https://doi.org/10.5194/acp-19-5993-2019>
265 doi: 10.5194/acp-19-5993-2019
- 266 He, M., Chau, J. L., Hall, C. M., Tsutsumi, M., Meek, C., & Hoffmann, P. (2018).
267 The 16-Day Planetary Wave Triggers the SW1-Tidal-Like Signatures During

- 268 2009 Sudden Stratospheric Warming. *Geophys. Res. Lett.*, *45*(22), 12,631–
269 12,638. Retrieved from <http://doi.wiley.com/10.1029/2018GL079798> doi:
270 10.1029/2018GL079798
- 271 He, M., Chau, J. L., Stober, G., Hall, C. M., Tsutsumi, M., & Hoffmann, P. (2017).
272 Application of Manley-Rowe Relation in Analyzing Nonlinear Interactions Be-
273 tween Planetary Waves and the Solar Semidiurnal Tide During 2009 Sudden
274 Stratospheric Warming Event. *J. Geophys. Res. Sp. Phys.*, *122*(10), 10,783–
275 10,795. Retrieved from <http://dx.doi.org/10.1002/2017JA024630> doi:
276 10.1002/2017JA024630
- 277 He, M., Chau, J. L., Stober, G., Li, G., Ning, B., & Hoffmann, P. (2018). Re-
278 lations Between Semidiurnal Tidal Variants Through Diagnosing the Zonal
279 Wavenumber Using a Phase Differencing Technique Based on Two Ground-
280 Based Detectors. *J. Geophys. Res. Atmos.*, *123*(8), 4015–4026. Retrieved
281 from [https://agupubs.onlinelibrary.wiley.com/doi/pdf/10.1002/](https://agupubs.onlinelibrary.wiley.com/doi/pdf/10.1002/2018JD028400)
282 [2018JD028400](http://doi.wiley.com/10.1002/2018JD028400)<http://doi.wiley.com/10.1002/2018JD028400> doi:
283 10.1002/2018JD028400
- 284 He, M., Hoffmann, P., Hall, C. M., Tsutsumi, M., & Chau, J. L. (2019). Predomi-
285 nant mesospheric transient Rossby normal modes prior to stratospheric sudden
286 warming events detected through a phase differencing technique. *Submitt. to*
287 *JGR*. doi: 10.1029/2019JD031599
- 288 Hedlin, M. A., de Groot-Hedlin, C. D., Forbes, J. M., & Drob, D. P. (2018). So-
289 lar Terminator Waves in Surface Pressure Observations. *Geophys. Res. Lett.*,
290 *45*(10), 5213–5219. doi: 10.1029/2018GL078528
- 291 Hibbins, R. E., Espy, P. J., Orsolini, Y. J., Limpasuvan, V., & Barnes, R. J. (2019).
292 SuperDARN Observations of Semidiurnal Tidal Variability in the MLT and
293 the Response to Sudden Stratospheric Warming Events. *J. Geophys. Res.*
294 *Atmos.*, *124*(9), 4862–4872. doi: 10.1029/2018JD030157
- 295 Isoda, F., Tsuda, T., Nakamura, T., Murayama, Y., Igarashi, K., Vincent, R. A.,
296 ... Manurung, S. L. (2002). Long-period wind oscillations in the mesosphere
297 and lower thermosphere at Yamagawa (32N, 131E), Pontianak (ON, 109E) and
298 Christmas Island (2N, 157W). *J. Atmos. Solar-Terrestrial Phys.*, *64*(8-11),
299 1055–1067. doi: 10.1016/S1364-6826(02)00057-3
- 300 Jacobi, C., Krug, A., & Merzlyakov, E. (2017). Radar observations of the quarterdi-

- 301 urnal tide at midlatitudes: Seasonal and long-term variations. *J. Atmos. Solar-*
 302 *Terrestrial Phys.*, 163, 70–77. Retrieved from [https://doi.org/10.1016/j](https://doi.org/10.1016/j.jastp.2017.05.014)
 303 .[jastp.2017.05.014](https://doi.org/10.1016/j.jastp.2017.05.014) doi: 10.1016/j.jastp.2017.05.014
- 304 Korotyshkin, D., Merzlyakov, E., Jacobi, C., Lilienthal, F., & Wu, Q. (2019). Lon-
 305 gitudinal MLT wind structure at higher mid-latitudes as seen by meteor radars
 306 at central and Eastern Europe (13E/49E). *Adv. Sp. Res.*, 63(10), 3154–3166.
 307 Retrieved from [http://www.sciencedirect.com/science/article/pii/](http://www.sciencedirect.com/science/article/pii/S0273117719300560)
 308 S0273117719300560 doi: 10.1016/j.asr.2019.01.036
- 309 Lilienthal, F., & Jacobi, C. (2019). Nonlinear forcing mechanisms of the terdiurnal
 310 solar tide and their impact on the zonal mean circulation. *Ann. Geophys. Dis-*
 311 *Discuss.*(April), 1–18. doi: 10.5194/angeo-2019-37
- 312 Lindzen, R. S., & Hong, S.-s. (1974). *Effects of Mean Winds and Horizon-*
 313 *tal Temperature Gradients on Solar and Lunar Semidiurnal Tides in*
 314 *the Atmosphere* (Vol. 31) (No. 5). Retrieved from [https://doi.org/](https://doi.org/10.1175/1520-0469(1974)031%3C1421:EOMWAH%3E2.0.CO;2)
 315 10.1175/1520-0469(1974)031%3C1421:EOMWAH%3E2.0.CO;2 doi:
 316 10.1175/1520-0469(1974)031%3C1421:eomwah%3E2.0.CO;2
- 317 Liu, H. L., Wang, W., Richmond, A. D., & Roble, R. G. (2010). Ionospheric vari-
 318 ability due to planetary waves and tides for solar minimum conditions. *J.*
 319 *Geophys. Res. Sp. Phys.*, 115(6), 1–13. Retrieved from [http://dx.doi.org/](http://dx.doi.org/10.1029/2009JA015188)
 320 10.1029/2009JA015188 doi: 10.1029/2009JA015188
- 321 Liu, M. H., Xu, J. Y., Yue, J., & Jiang, G. Y. (2015). Global structure and seasonal
 322 variations of the migrating 6-h tide observed by SABER/TIMED. *Sci. China*
 323 *Earth Sci.*, 58(7), 1216–1227. doi: 10.1007/s11430-014-5046-6
- 324 McLandress, C. (2002). The seasonal variation of the propagating diurnal
 325 tide in the mesosphere and lower thermosphere. Part II: The role of tidal
 326 heating and zonal mean winds. *J. Atmos. Sci.*, 59(5), 907–922. doi:
 327 10.1175/1520-0469(2002)059%3C0907:TSVOTP%3E2.0.CO;2
- 328 Miyahara, S., & Forbes, J. M. (1991). Interactions between gravity waves and the
 329 diurnal tide in the mesosphere and lower thermosphere. *J. Meteorol. Soc.*
 330 *Japan*, 69(5), 523–531. doi: 10.2151/jmsj1965.69.5.523
- 331 Miyoshi, Y., Fujiwara, H., Forbes, J. M., & Bruinsma, S. L. (2009). Solar termina-
 332 tor wave and its relation to the atmospheric tide. *J. Geophys. Res. Sp. Phys.*,
 333 114(7), 1–14. doi: 10.1029/2009JA014110

- 334 Pancheva, D., Merzlyakov, E., Mitchell, N. J., Portnyagin, Y., Manson, A. H., Ja-
 335 cobi, C., . . . Oleynikov, A. N. (2002). *Global-scale tidal variability during*
 336 *the PSMOS campaign of June-August 1999: Interaction with planetary waves*
 337 (Vol. 64) (No. 17). doi: 10.1016/S1364-6826(02)00199-2
- 338 Pedatella, N. M., & Forbes, J. M. (2010, jun). Evidence for stratosphere sudden
 339 warming-ionosphere coupling due to vertically propagating tides. *Geophys.*
 340 *Res. Lett.*, *37*(11), n/a–n/a. Retrieved from [http://doi.wiley.com/10.1029/](http://doi.wiley.com/10.1029/2010GL043560)
 341 [2010GL043560](http://doi.wiley.com/10.1029/2010GL043560) doi: 10.1029/2010GL043560
- 342 Pogoreltsev, A. I., Pancheva, D., & Mitchell, N. J. (2002). Secondary planetary
 343 waves in the middle atmosphere: Numerical simulation and analysis of the
 344 neutral wind data. *J. Atmos. Solar-Terrestrial Phys.*, *64*(8-11), 1251–1261.
 345 doi: 10.1016/S1364-6826(02)00039-1
- 346 Reed, R. (1963). On the cause of the stratospheric sudden warming phenomenon.
 347 *Meteorol. Abhand.*, *36*, 315–334.
- 348 Scherhag, R. (1952). Die explosionsartigen Stratosphärenwärmungen des
 349 Spätwinters 1951/52. *Berichte des Dtsch. Wetterdienstes der US-Zone*, *6*(38),
 350 51–63.
- 351 Singer, W., Hoffmann, P., Kishore Kumar, G., Mitchell, N. J., & Matthias, V.
 352 (2013). Atmospheric Coupling by Gravity Waves: Climatology of Grav-
 353 ity Wave Activity, Mesospheric Turbulence and Their Relations to Solar
 354 Activity. In F.-J. Lübken (Ed.), *Clim. weather sun-earth syst. highlights*
 355 *from a prior. progr.* (pp. 409–427). Dordrecht: Springer Netherlands. Re-
 356 trieved from https://doi.org/10.1007/978-94-007-4348-9_{_}22 doi:
 357 [10.1007/978-94-007-4348-9.22](https://doi.org/10.1007/978-94-007-4348-9.22)
- 358 Smith, A. K. (2012). Global Dynamics of the MLT. *Surv. Geophys.*, *33*(6), 1177–
 359 1230. Retrieved from <http://dx.doi.org/10.1007/s10712-012-9196-9> doi:
 360 [10.1007/s10712-012-9196-9](https://doi.org/10.1007/s10712-012-9196-9)
- 361 Smith, A. K., Pancheva, D. V., & Mitchell, N. J. (2004). Observations and mod-
 362 eling of the 6-hour tide in the upper mesosphere. *J. Geophys. Res. D Atmos.*,
 363 *109*(10), 1–11. doi: 10.1029/2003JD004421
- 364 Truskowski, A. O., Forbes, J. M., Zhang, X., & Palo, S. E. (2014). New perspectives
 365 on thermosphere tides: 1. lower thermosphere spectra and seasonal-latitudinal
 366 structures. *Earth, Planets Sp.*, *66*(1), 1–17. doi: 10.1186/s40623-014-0136-4

- 367 Walker, S. N., Sahraoui, F., Balikhin, M. A., Belmont, G., Pinçon, J. L., Rezeau,
368 L., . . . André, M. (2004). A comparison of wave mode identification
369 techniques. *Ann. Geophys.*, *22*(8), 3021–3032. Retrieved from [https://](https://www.ann-geophys.net/22/3021/2004/)
370 www.ann-geophys.net/22/3021/2004/ doi: 10.5194/angeo-22-3021-2004
- 371 Won, Y. I., Wu, Q., Cho, Y. M., Shepherd, G. G., Killeen, T. L., Espy, P. J., . . .
372 Solheim, B. (2003). Polar cap observations of mesospheric and lower ther-
373 mospheric 4-hour waves in temperature. *Geophys. Res. Lett.*, *30*(7), 10–
374 13. Retrieved from <http://dx.doi.org/10.1029/2002GL016364> doi:
375 10.1029/2002GL016364
- 376 Xiong, J., Wan, W., Ding, F., Liu, L., Ning, B., & Niu, X. (2013, may). Cou-
377 pling between mesosphere and ionosphere over Beijing through semidiurnal
378 tides during the 2009 sudden stratospheric warming. *J. Geophys. Res. Sp.*
379 *Phys.*, *118*(5), 2511–2521. Retrieved from [http://doi.wiley.com/10.1002/](http://doi.wiley.com/10.1002/jgra.50280)
380 [jgra.50280](http://doi.wiley.com/10.1002/jgra.50280) doi: 10.1002/jgra.50280
- 381 Xu, J., Smith, A. K., Jiang, G., Yuan, W., & Gao, H. (2012). Features of the sea-
382 sonal variation of the semidiurnal, terdiurnal and 6-h components of ozone
383 heating evaluated from Aura/MLS observations. *Ann. Geophys.*, *30*(2), 259–
384 281. doi: 10.5194/angeo-30-259-2012
- 385 Yu, Y., Wan, W., Ning, B., Liu, L., Wang, Z., Hu, L., & Ren, Z. (2013). Tidal
386 wind mapping from observations of a meteor radar chain in December 2011. *J.*
387 *Geophys. Res. Sp. Phys.*, *118*(5), 2321–2332. Retrieved from [https://agupubs](https://agupubs.onlinelibrary.wiley.com/doi/abs/10.1029/2012JA017976)
388 [.onlinelibrary.wiley.com/doi/abs/10.1029/2012JA017976](https://agupubs.onlinelibrary.wiley.com/doi/abs/10.1029/2012JA017976) doi: 10.1029/
389 2012JA017976
- 390 Zhang, X., & Forbes, J. M. (2014, dec). Lunar tide in the thermosphere and weaken-
391 ing of the northern polar vortex. *Geophys. Res. Lett.*, *41*(23), 8201–8207. Re-
392 trieved from <http://doi.wiley.com/10.1002/2014GL062103> doi: 10.1002/
393 2014GL062103

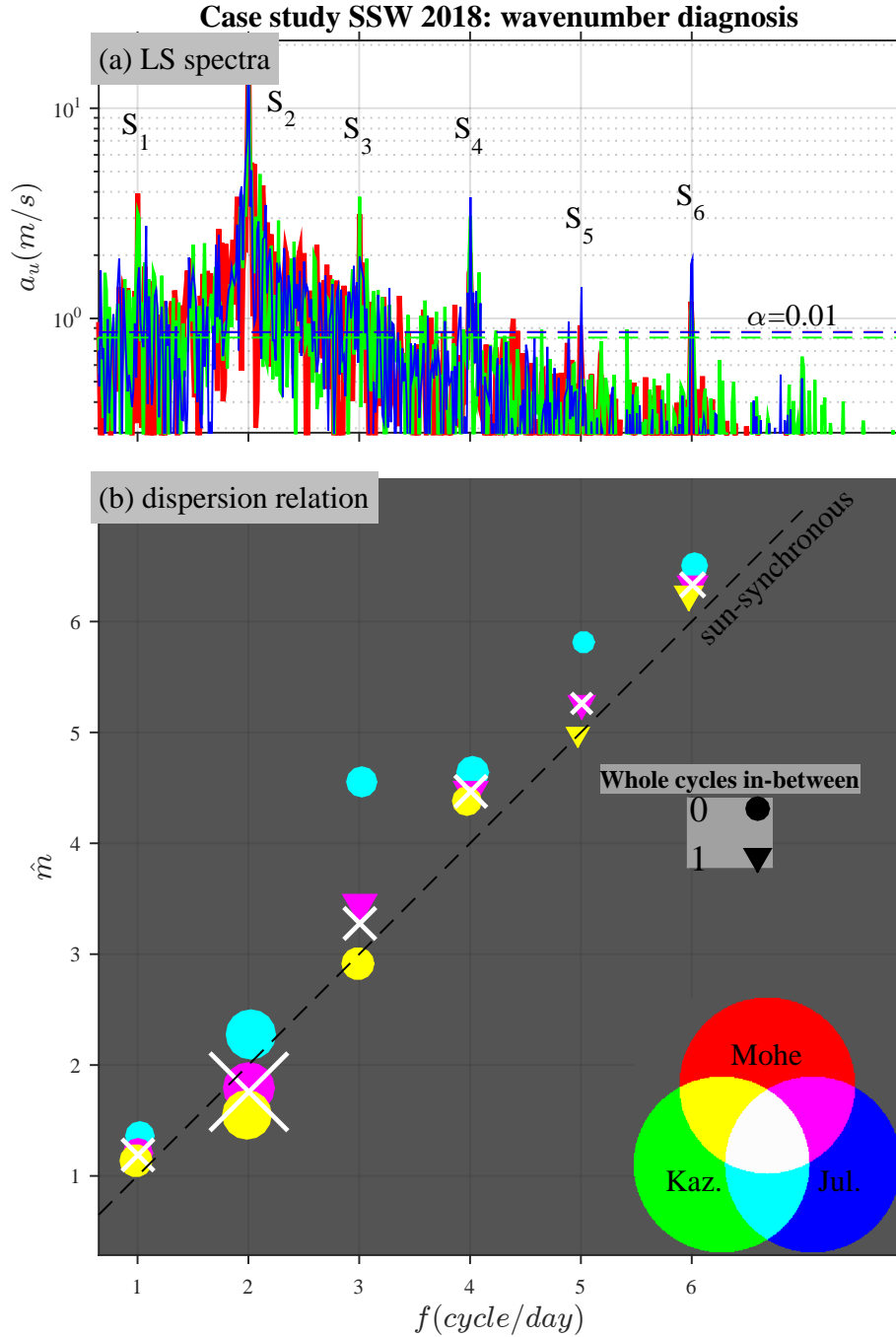


Figure 1: (a) Lomb-Scargle periodograms of the mesospheric zonal wind over Mohe, Kazan, and Juliusruh, at 90 km altitude between 30 November 2017 and 15 February 2018. (b) Dispersion relation of oscillations at periods of solar-day harmonics through dual-station PDT (colored elements) and triple-station LS approach (white crosses). The dashed line represents the phase velocity $v_p = f/m = 360^\circ/day$ in longitude. Referring to the color code on the right bottom of (b), the primary colors (red, green and blue in (a)) and their secondary colors (cyan, magenta and yellow in (b)) denote three single radars and three of their pairs, respectively.

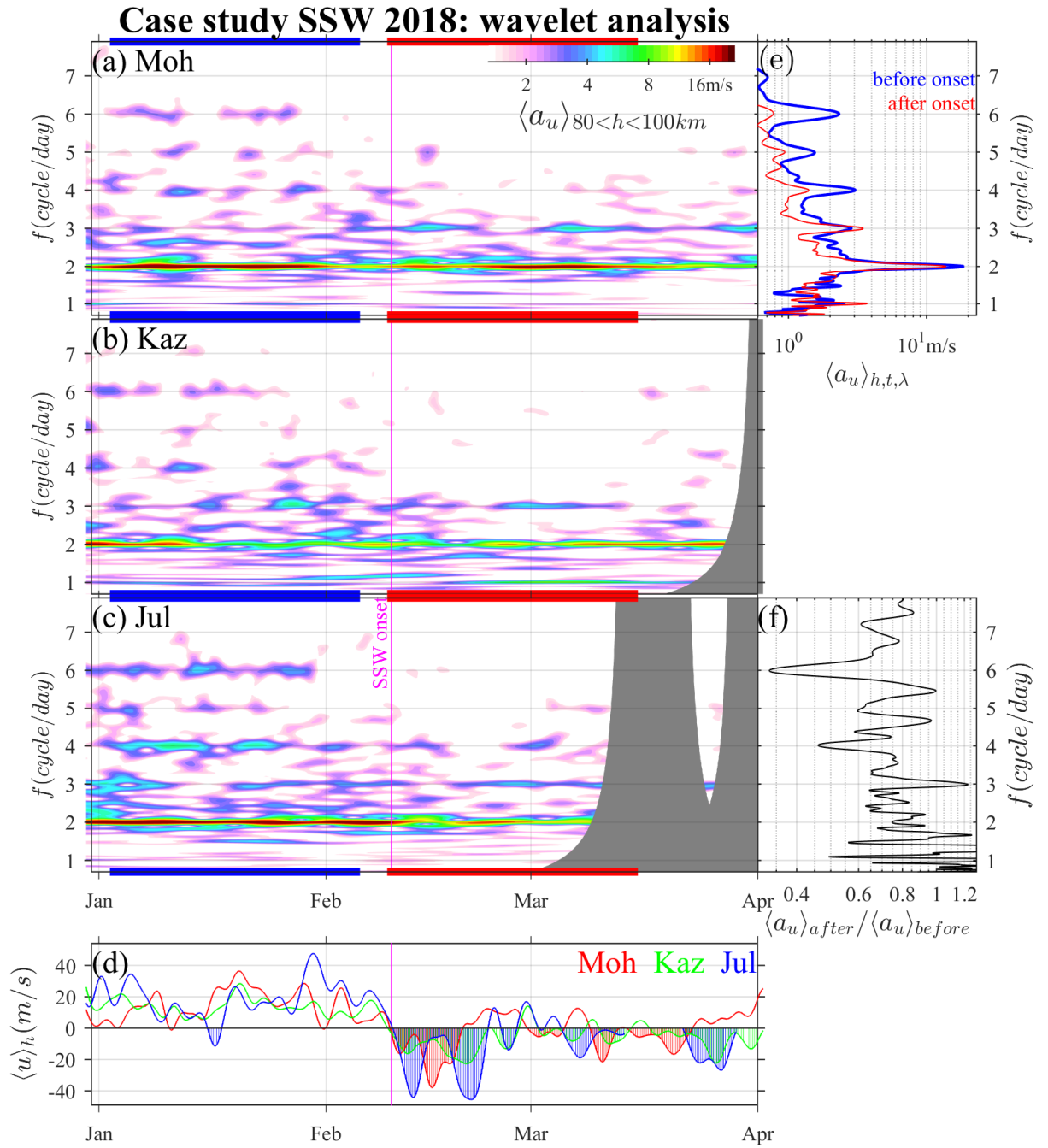


Figure 2: Wavelet spectra of the mesospheric zonal wind over (a) Mohe, (b) Kazan, and (c) Juliusruh, in early 2018. (d) Low-pass filtered zonal wind. (e) Temporally-averaged spectra within the time windows color-indicated by the blue and red segments in (a-c). (f) The ratio of the read of the red line over that of the blue in (e). (a-d) are the average of the corresponding results at individual attitudes between 80-100 km.

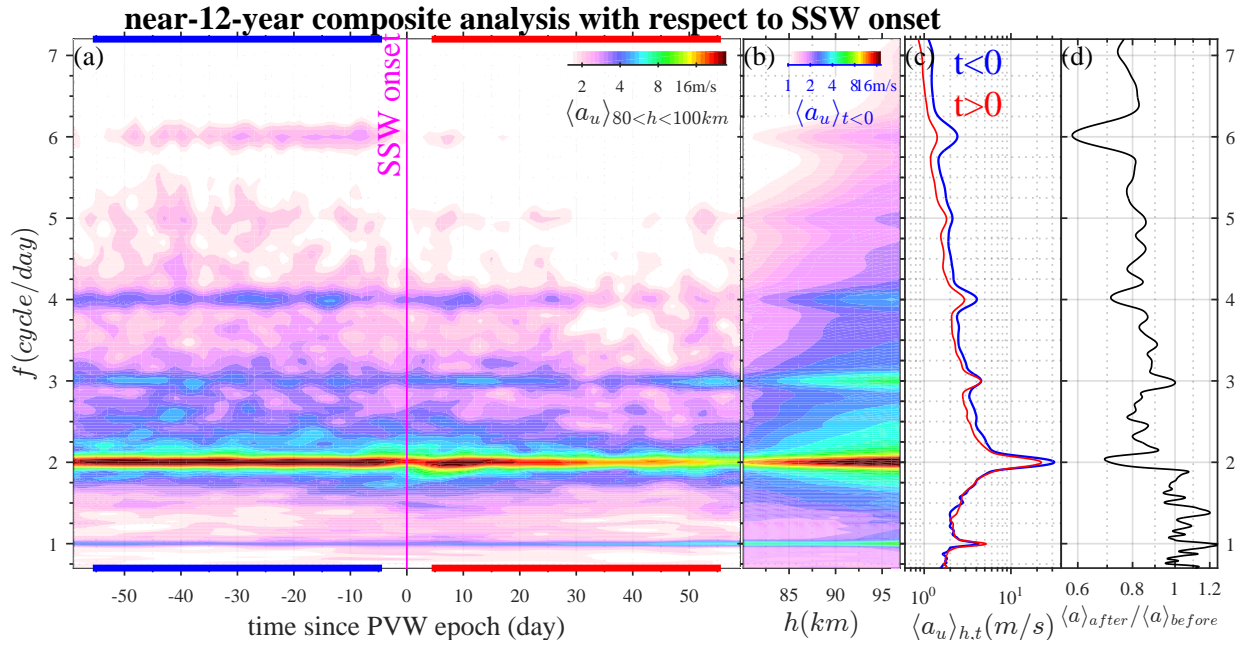


Figure 3: (a) Composite analysis of altitude-averaged (over 80-100 km) wavelet spectrum of the zonal wind over Juliusruh with respect to SSW onsets referring to the PVWs. (b) The wavelet spectrum averaged in the time window indicated by the blue lines before the onset in (a). (c) Temporal average of (a) within the time window indicated by the blue and red lines in (a). (d) The ratio between the red and the blue lines in (c).

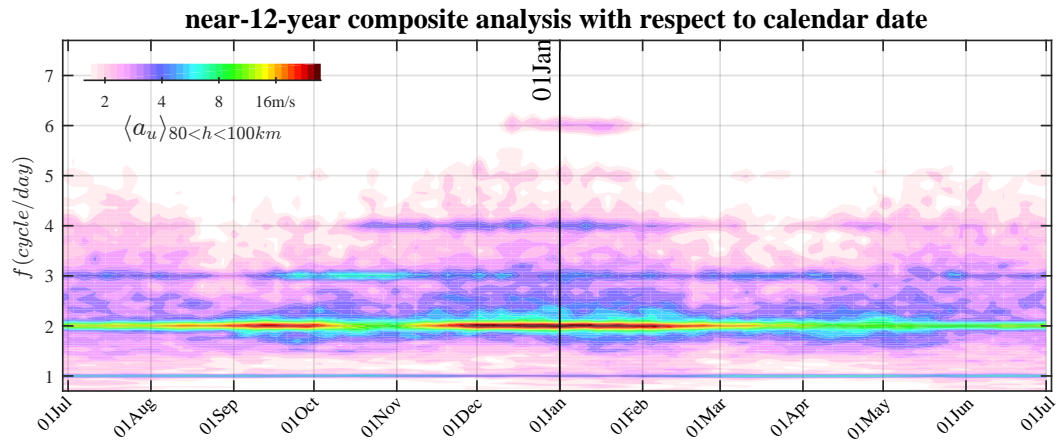


Figure 4: Same plot as Figure 3a, but averaged with respect to calendar date.

394 **Appendix A Approaches for wavenumber diagnosis**

395 **A1 A dual-station approach**

Ground-based radars provided long continuous records of mesospheric winds but are available only at a limited number of sites. Radars can hardly compose a functional network for exploring the horizontal scale of global-scale waves, but do provide high spatial and temporal information on local dynamics. Efforts have been made in the past to join two zonally aligned detectors to diagnose the zonal scale of waves through analyzing the phase variations of the wave-like oscillations (e.g., Clark et al., 2002; Pogoreltsev et al., 2002; Won et al., 2003). Recently, this approach was consolidated into a compact method, called the phase differencing technique (PDT He, Chau, Stober, et al., 2018; He, Chau, Hall, et al., 2018; He et al., 2019), in which PDT was used to explore a variety of waves. As summarized in, e.g., Equation 19 in He, Chau, Stober, et al. (2018), if a single wave with an unknown zonal wavenumber m at given frequency f is coherently detected at two longitudes λ_1 and λ_2 with amplitudes \tilde{a}_1 and \tilde{a}_2 , then m has a solution,

$$m = \frac{\arg\{\tilde{a}_2^* \tilde{a}_1\} + 2C\pi}{\lambda_1 - \lambda_2} \quad (\text{A1})$$

396 Here, \tilde{a}_1 and \tilde{a}_2 could be estimated from spectral analysis as in Figure 1a; and $C \in \mathbb{Z}$
 397 represents the whole-cycle ambiguity. To deal with the ambiguity, traditional approaches
 398 required that the underlying wavelengths are long enough so that $C = 0$ (e.g., Walker
 399 et al., 2004; Isoda et al., 2002) which was released to $C \in \{-1, 0, 1\}$ through assum-
 400 ing $m \in \mathbb{Z}$ (e.g., Equation 14 He, Chau, Stober, et al., 2018). Here, the three radars
 401 allow us to release the C further conservatively and subjectively to $C \in C_c := \{-1, 0, 1, \dots, 10\}$.
 402 Note that the maximum possible C_c is different at harmonic as discussed in the end of
 403 current Section.

The three radars compose three combinations of radar pairs, $k = 1, 2, 3$, allowing three solutions $m_k(C)$ for each $C \in C_c$ at each frequency according to Equation A1. If only one wave m exist (namely, satisfies the single wave assumption, cf, He, Chau, Hall, et al., 2018), then $m_k(C_k)$ from the three pairs should converge, namely, C_1^m, C_2^m , and C_3^m exist so that $m_1(C_1^m) = m_2(C_2^m) = m_3(C_3^m)$ or their variance $\sigma^2(m_k(C_k^m)) := \sum_k (m_k - \bar{m}_k)^2 / 3 = 0$. C_k , and m_k can be optimized through minimizing $\sigma^2(m_k)$,

$$\hat{C}_k^m = \underset{C_k^m \in C_c}{\operatorname{argmin}} \sigma^2(m_k) \quad (\text{A2})$$

404 The resultant $\hat{m}_k(C_k^m)$ is displayed in Figure 1b, in which three colors, yellow, magenta
 405 and cyan, of the symbols represent $k=1,2,3$, while the circular and triangle shapes rep-
 406 resent $C_k^m=0$ and 1, respectively.

407 In Figure 1b and at most harmonics, the separation between the cyan symbol and
 408 any of the other two is larger than the separation between the other two, which might
 409 due to the associated longitudinal difference, i.e., between Kazan and Juliusruh, is smaller
 410 that the longitudinal difference of other pairs. A smaller separation in longitude, accord-
 411 ing to Equation A1, will be associated with a larger uncertainty in the wavenumber es-
 412 timation. Besides, in Figure 1b the estimations at S3 and S5 do not converge as good
 413 as those at the rest harmonics, which might due to the relative intensity (the ratio be-
 414 tween tidal peak and the background noise) is lower at S3 and S5 than at other harmon-
 415 ics. The relative intensity might affect the maximum possible C_c defined subjectively above.
 416 For example, if we expand C_c in Equation A2 to $\{-1, 0, \dots, 27\}$, the estimation \hat{m}_k varies
 417 at S3 and S5, but not at the rest four harmonics.

418 **A2 A triple-station approach**

Following, e.g., Equation 1 in He and Chau (2019), the complex amplitude \tilde{a}_k of
 an oscillation due to a single zonally traveling wave with wavenumber m detected by a
 radar at longitude λ_k , $k=1,2,3$, could be represented as $\tilde{a}_k = \tilde{a}_0 e^{i2\pi m \lambda_k}$. The estima-
 tion of \tilde{a}_k in Figure 1a allows estimating $\tilde{a}_o(m)$ at arbitrary m through a least square
 regression, denoted as $\hat{\tilde{a}}_o(m)$. We estimate $\hat{\tilde{a}}_o(m)$ on a candidate grid $m \in M_s = \{-1, -0.9, -$
 $0.8, \dots, 70$, and optimize m through

$$\hat{m}^T = \operatorname{argmin}_{m \in M_s} \sum_k |\tilde{a}_k - \hat{\tilde{a}}_o(m) e^{i2\pi m \lambda_k}|^2 \quad (\text{A3})$$

419 where the superscript 'T' denotes triple-station analysis. The optimization results are
 420 displayed in Figure 1b as white crosses. Note that as the selection of C_c in the previous
 421 section, M_s is preassigned subjectively, and at most harmonics the estimation will still
 422 stand in a broader M_s range.